The "MASSIVE" brain dataset: Multiple Acquisitions for Standardization of Structural Imaging Validation and Evaluation

Martijn Froeling (1), Chantal M.W. Tax (2), Sjoerd B. Vos (2,3), Peter R. Luijten (1), and Alexander Leemans (2)

(1) Department of Radiology, University Medical Center Utrecht, Utrecht, Netherlands

(2) Image Sciences Institute, University Medical Center Utrecht, Utrecht, Netherlands

(3) Translational Imaging Group, CMIC, University College London, London, United Kingdom

Corresponding author:

Martijn Froeling

Department of Radiology

University Medical Center Utrecht

Heidelberglaan 100,

3584 CX Utrecht

The Netherlands

Tel: (+31) 88 75 53 305

e-Mail: m.froeling@umcutrecht.nl

Word Count: 3602

Abstract

Purpose: In this work we present the MASSIVE (Multiple Acquisitions for Standardization of Structural Imaging Validation and Evaluation) brain dataset of a single healthy subject, which is intended to facilitate diffusion MRI (dMRI) modeling and methodology development.

Methods: MRI data of one healthy subject (female, 25 y) were acquired on a clinical 3 T system (Philips Achieva) with an 8-channel head coil. In total, the subject was scanned on 18 different occasions with a total acquisition time of 22.5 hours. The dMRI data were acquired with an isotropic resolution of 2.5 mm^3 and distributed over five shells with b-values up to 4000 s/mm^2 and two Cartesian grids with b-values up to 9000 s/mm^2.

Results: The final dataset consists of 8000 dMRI volumes, corresponding B_0 field maps and noise maps for subsets of the dMRI scans, and ten 3D FLAIR, T_1-, and T_2-weighted scans. The average signal-to-noise-ratio (SNR) of the non-diffusion-weighted images was roughly 35.

Conclusion: This unique set of in vivo MRI data will provide a robust framework to evaluate novel diffusion processing techniques and to reliably compare different approaches for diffusion modeling. The MASSIVE dataset is made publically available (both unprocessed and processed) on *www.massive-data.org*.

Keywords

Diffusion MRI, structural MRI, modeling, methods development, evaluation, brain dataset.

Introduction

Diffusion magnetic resonance imaging (dMRI) is used in a wide range of clinical and scientific disciplines for its ability to infer information about tissue architecture and microstructure in vivo (1–4). Investigating brain tissue characteristics with dMRI, however, remains challenging mainly due to the presence of numerous artifacts during data acquisition and the high complexity of the diffusion-weighted (DW) signal for modeling purposes. Consequently, multiple processing steps have to be performed to be able to extract meaningful and reliable features from dMRI data. A variety of correction strategies have been developed that address data imperfections (e.g., eddy current induced distortions, susceptibility based deformations caused by magnetic field inhomogeneities, noise and physiological artifacts (1,5)) to minimize the presence of confounds that could convolute data interpretation. In addition, a wide range of dMRI models and reconstruction methods have been proposed that aim to extract tissue characteristics in a reliable way, including diffusion tensor imaging (DTI) (6), diffusion kurtosis imaging (DKI) (7), diffusion spectrum imaging (DSI) (8), Q-ball imaging (QBI) (9), spherical deconvolution (SD) (10–12), CHARMED (13), and NODDI (14).

Notwithstanding recent developments in dMRI artifact correction and modeling, optimizing the dMRI processing pipeline is still an active area of research. For example, there is currently no consensus on the optimal dMRI model or representation to characterize the DW signal, or on the optimal sampling scheme for dMRI reconstruction techniques that use ´multi-shell´ acquisitions (i.e., gradient directions distributed over multiple b-value shells). Moreover, these two issues may even depend on each other, i.e., optimal sampling might be different for different models. In parallel, many new artifact correction strategies are currently being developed (15,16). In this context, a comprehensive evaluation framework for such novel diffusion processing techniques and for a reliable comparison between different approaches is highly desired.

Unbiased and reliable evaluations are, however, generally hampered by the lack of a genuine gold-standard, and there is an urgent need for a reliable framework that can facilitate the development of dMRI methodology. Hardware phantoms and simulations are very valuable because of their known ground truth, but are often too simplistic (17) or can be biased towards a specific model (18–20). Real data acquisitions can, despite their unknown ground-truth, serve as valuable references to complement phantom and simulated data in the validation and evaluation of new processing strategies. For this purpose, a comprehensive dMRI dataset is required.

Data repositories and databases are becoming more readily available (21), greatly facilitating the development of dMRI methods. Many of these repositories contain cross-sectional and/or longitudinal data allowing for research on normal brain development and function (22–26). Other databases aim to give insight into brain anatomy and resolve complex neuronal microarchitecture, either by deriving templates or atlases from data of a single subject or multiple subjects (27–30), or using high resolution post mortem data (31–33). An example of a cross-sectional repository is the Human Connectome Project (HCP) database, which will contain dMRI data (among others) of 1200 subjects acquired with maximum gradient strengths surpassing that of clinical scanners (25,26). Although this database contains data acquired with multiple b-values and more diffusion gradient directions than most acquisitions it is still limited in its sampling of q-space (270 directions on three shells). More densely sampled q-space data (512 directions) with higher b-values (b=10.000 s/mm^2) for a broader age range are also available (34). These datasets are acquired with innovative gradient systems and therefore not comparable to those typically acquired in a clinical setting in terms of resolution and SNR, among others. Another dMRI database is provided as part of the "MyConnectome Project" (35). This database contains 19 (15 usable) repeated scans of a single subject acquired over the course of 18 months with the purpose of specifically investigating the dynamics of brain function, and the scans are thus identical in terms of acquisition parameters (i.e., b-values and gradient orientations). Despite the availability of many excellent high quality

repositories, for validation of processing methods and algorithms (36,37) in a clinical setting, typically, synthetic phantoms (20,38,39) or small clinical datasets (40) are still used.

In this work we present the MASSIVE (Multiple Acquisitions for Standardization of Structural Imaging Validation and Evaluation) brain dataset containing multi-modal MR data and 8000 dMRI volumes of a single healthy subject acquired on a clinical 3 T scanner. All the datasets were specifically acquired in a clinical setting, i.e., using single-shot echo-planar imaging (EPI), `conventional` gradient strengths and hardware, no dedicated head fixation or advanced high density receive coil, to be in line with the current standards in acquisition protocols from routine examinations. As such, subsets of the MASSIVE dataset are comparable to data acquired in clinical studies, and can serve as representative test beds for new developments in a wide range of dMRI data correction strategies, image processing techniques, and microstructural modeling approaches. The MASSIVE dataset consists of 8000 dMRI volumes with b-values up to 9000 s/mm^2, sampled in configurations of five shells and two Cartesian grids. Data was acquired with echo-planar imaging (EPI) phase-encoding in both anterior-posterior (AP) and posterior-anterior (PA) directions, and with gradient directions both in positive and negative z-direction resulting in 2000 scans for each combination. In addition, the dataset contains B_0 field maps, noise maps, and ten 3D fluid-attenuated inversion recovery (FLAIR), T_1-, and T_2-weighted datasets, which often play an important role in dMRI processing and analysis methods (e.g., (41–43)) and can also be used independently for test-retest experiments and methodological evaluations and comparisons (e.g., (44–46)). The MASSIVE dataset, which was first presented at the 22nd Scientific Annual Meeting of the ISMRM (47), is made publicly available on *www.massive-data.org*.

Methods

Data acquisition

All the MRI data of the healthy subject (female, 25 y) were acquired on a clinical 3 T system (Philips Achieva) with an 8-channel head coil. The subject gave informed consent to participate in this study under a protocol approved by the University Medical Center Utrecht ethics board. In total, the subject was scanned on 18 different occasions (total acquisition time: 22.5 h). A schematic overview of the protocol for a single session is shown in **Figure 1**. Each of the 18 scan sessions consisted of four dMRI acquisition blocks of 15 minutes in which a unique subset of the 8000 DW volumes was acquired with B_0-maps being acquired before and after each of these four dMRI acquisition block (48–50). Additionally, noise maps were obtained at the end of each dMRI acquisition block by switching off the RF pulses and imaging gradients. Finally, ten 3D FLAIR, T_1-, and T_2-weighted datasets were acquired in five of the eighteen sessions. In these sessions, two FLAIR, T_1-, and T_2-weighted datasets were acquired with a two hour pause in between. Positioning of the head in the coil and planning the field-of-view in each session was done manually, which resulted in small offsets in rotation and translation. The coronal positioning was intentionally varied between sessions to minimize the systematic effects of ghosting artifacts. The design of the diffusion and anatomical MRI acquisitions will be outlined in more detail in the next paragraphs (further acquisition details can be found in **Table 1**).

Diffusion MRI

The MASSIVE dataset comprises 8000 unique DW volumes, subdivided into four 'sets' with both positive and negative gradient directions, and with both AP and PA phase encoding directions (in the following referred to as AP+, AP-, PA+ and PA-). The acquisition of each set of 2000 DW volumes was divided in 18 sessions (see examples shown in **Figure 2**) of which eight sessions contained 120 dMRI

volumes and 10 sessions contained 104 dMRI volumes. The ordering of the diffusion gradient orientations and b-values was randomized throughout every set to prevent an acquisition bias across sessions (**Figure 2 D-F**). The exact scan order can be found in the lookup table which can be downloaded from the website www.massive-data.org.

The gradient directions are distributed over five shells and two Cartesian grids. The diffusion gradient orientations on the shells were generated using the approach described in Caruyer et al., 2013 (51). In short, this approach uses static repulsion of particles to homogenize the gradient orientations on half a sphere (51–53). In this work, the solution was obtained by an iterative solver where in each iteration the particles repel each other and are subsequently back-projected onto the unit sphere until convergence is reached (see **Supporting material 1, Figure S1**). The software tool that was developed for computing these gradient orientations is also made available on the MASSIVE website.

The five shells consisted of 125, 250, 250, 250 and 300 gradient orientations on the half sphere with a b-value of 500, 1000, 2000, 3000 and 4000 s/mm^2, respectively. The two Cartesian grids were evenly spaced in half a cube, one with an even ($8^3/2 = 256$) and one with an odd ($(9^3+1)/2 = 365$) number of samples. The maximum b-values along the axes were 2296 s/mm^2 (q = 0.038 μm^{-1}) for the even grid and 3000 s/mm^2 (q = 0.043 μm^{-1}) for the uneven grid. The maximum b-values for the corner points were 6890 s/mm^2 (q = 0.066 μm^{-1}) for the even grid and 9000 s/mm^2 (q = 0.075 μm^{-1}) for the uneven grid. For the diffusion data with a b>3000 s/mm^2 and for the Cartesian grids the EPI bandwidth was reduced from 50 to 30 Hz (keeping the TE, δ and Δ constant) to maximize the SNR for the high b-values and to be able to acquire the data in a feasible scan time given the system's duty cycle limitations. Additionally, 204 b = 0 s/mm^2 images were acquired, resulting in the 2000 dMRI volumes per set with approximately a 1:9 ratio between the non-DW and the DW volumes. These non-DW volumes were randomly interleaved throughout each dMRI acquisition to avoid any measurement bias and to allow for signal drift correction ((16), see also section 2.2).

Anatomical MRI

Ten anatomical MRI datasets (T_1- and T_2-weighted, and FLAIR) were acquired as they often support dMRI processing and analysis methods (facial features were removed for anonymization). For instance, T_1-weighted data can be used for segmentation of gray and white matter regions, which can be used to improve fiber tractography (43,54). Similarly, as T_2-weighted data provide a comparable contrast with the non-DW data, these can be used to correct for susceptibility induced distortions (41,42). The FLAIR data, which has a similar contrast to the T_2-weighted data but with suppression of the signals originating from the cerebrospinal fluid, may be useful to investigate the contributions of partial volume effects (55,56). Details of the acquisition protocols for these anatomical MRI data are included in **Table 1**.

Data processing

In addition to the raw data, we provide further information on the acquired data, such as SNR estimates and the "true" applied b-matrix for the raw data as derived from the scanner. In addition, we make available three processed datasets: 1) only the intensity-normalized data; 2) both intensity-normalized and signal-drift corrected data; and 3) data that has been intensity-normalized and corrected for signal-drift, subject motion, eddy current distortions, and EPI deformations. Note that for each of these results conventional processing tools were used as described in the following subsections.

Signal-to-noise-ratio (SNR) estimation

Having knowledge of the image SNR is often important in dMRI modeling and processing (1,57–64). The SNR can be quantified in numerous ways, however, and may not be the same across different methods (65–69). Therefore, noise maps were obtained after each acquisition of a 15-minute

diffusion block, by switching off the gradients and RF power but leaving the acquisition channels open. The acquisition parameters of the noise map were equal to the dMRI acquisition parameters and, as such, an accurate noise measurement is obtained. To calculate a rough approximation for the global SNR, the average whole brain signal within a mask was computed for every DW volume and divided by the noise standard deviation within the same brain mask as derived from the noise map.

Intensity normalization and signal drift correction

Since the data were acquired in different sessions, intensity normalization between sessions is needed to be able to combine the DW volumes into a single data set (70). To this end, the first volume of each 15-minute dMRI acquisition block, which was always a non-DW volume, was used to normalize the signal intensities of all the other volumes within that acquisition block.

In dMRI, the heavy duty cycle of the EPI-readout and the diffusion gradients can lead to temporal instability of the scanner. This instability typically causes a decrease in global signal intensity of the DW images over time, as explained in detail in (16). To correct for this so-called signal drift, the non-DW volumes, which were randomly interleaved throughout each dMRI acquisition block, were identified. Subsequently, the signal drift that occurred during this 15 minute time-window was characterized by a quadratic fit of the mean signal of the b=0 s/mm^2 volumes as a function of the scanned volume (16), i.e.

$$S(n\,|b = 0\ \mathrm{s/mm}) = d_1 \cdot n^2 + d_2 \cdot n + S_0, \qquad (1)$$

where S is the normalized measured signal, n the ordering number of the acquired volume, S_0 the signal offset at $n = 0$, and d_1 and d_2 describe the quadratic and linear signal drift per volume, respectively. The corrected signal of the nth volume, $S_{cor}(n)$, is then given by:

$$S_{cor}(n) = \alpha\ \frac{S(n)}{d_1 \cdot n^2 + d_2 \cdot n + S_0}, \qquad (2)$$

where the factor α is an arbitrary chosen signal scaling factor.

True b-matrix calculation

In addition to the DW pulsed field gradients, imaging gradients can also contribute to the diffusion-weighting. Therefore, the actual b-matrix was calculated in addition to the prescribed b-matrix (71,72). The amount of diffusion weighting $\boldsymbol{b}_{i,j}$ along the coordinate axes $i = \{x, y, z\}$ and $j = \{x, y, z\}$ can be expressed as the time (t) integral over the echo time (TE) of the zeroth-order ($n = 0$) moments ($\boldsymbol{M}_n$) of the gradients, i.e.,

$$\boldsymbol{b}_{i,j} = \gamma^2 \int_0^{TE} \boldsymbol{M}(t)_{\mathrm{n}=0,i} \boldsymbol{M}(t)_{\mathrm{n}=0,j} dt, \quad (3)$$

with,

$$M(t)_n = \int_0^t t'^n G(t) dt', \quad (4)$$

Where γ is the gyromagnetic ratio and $G(t)$ the gradient wave form.

Correcting for subject motion, eddy current distortions, and EPI deformations

dMRI acquisitions suffer from subject motion and eddy current induced distortions within an acquisition session (1,73). In this study, the dataset was scanned in multiple sessions which caused an additional source of misalignment. As a result, the final gradient distribution will slightly differ from the applied one, because the b-matrix needs to be rotated when correcting for subject motion (74). For each session, the dMRI data was registered using ExploreDTI (75) using an affine method with 12 degrees of freedom to also correct for eddy current induced distortions in the same step (76). The first b=0 s/mm^2 image of each acquisition was chosen as a reference image. To correct for EPI distortions and subject motion between the different session, all data was transformed to a common

T_1-weighted anatomical target dataset using a rigid-registration for rough alignment, followed by a non-rigid b-spline registration to correct for susceptibility induced deformations (42,77–79). Here, only non-rigid deformations along the phase-encoding axis of the dMRI data were allowed, as this is the axis along which susceptibility distortions occur. Note that the transformations from these two last steps are combined with the previous eddy current correction procedure to ensure that only one interpolation step is needed minimizing unwanted smoothing effects due to resampling All other anatomical datasets (FLAIR, T_1-, and T_2-weighted) were also transferred to the same T_1-weighted target dataset using rigid registration.

Results

Figure 3 shows representative images of the acquired data. The top two rows (**Figure 3 A-H**) show images from the different shells and Cartesian grids. The FLAIR, T_1-, and T_2-weighted anatomical scans are shown in **Figure 3 I-K** and a B_0 map is shown in **Figure 3 L**.

Signal-to-noise-ratio (SNR)

The noise as derived from the noise map is Rayleigh distributed (see **Figure 4 A**). The SNR estimates are presented in **Figure 4 B**. The average SNR was between 35 and 40 for the non-DW images and was in the same range across all sessions. The SNR of the data in sessions 9 to 18 ($b = 4000$ s/mm^2 shell and both DSI grids) was around 15 percent higher than for the shells with $b \leq 3000$ s/mm^2, which was to be expected with the lower bandwidth. The estimated SNR values per acquired volume can be found in the lookup table which can be downloaded from the website www.massive-data.org.

Intensity normalization and signal drift correction

In **Figure 5**, the mean signal of the non-DW volumes is shown as a function of the measurement number (red markers) for 24 randomly chosen acquisition blocks. The quadratic fit used to correct for signal drift is shown in black and the signal-drift corrected data are shown in blue. The mean signal drift during a 15 minute acquisition block was 9.3% with a standard deviation of 3.7% (range: 3.0 to 18.8 %) with respect to the initial volume. The mean signal for all the 8000 acquired volumes is shown in **Figure 6 A** and **B**. By comparing **A** with **B** of **Figure 6**, one can appreciate that the mean signal of the normalized and drift-corrected volumes across all sessions is more constant now.

True b-matrix calculation

Since the slice selection gradients are always in the orientation of the z-axis, the actual b-value for the non-DW images, using **equations [3]** and **[4]**, is 0.25 s/mm^2 instead of 0 s/mm^2. The average value and the range of the actual b-values of the five shells are listed in **Table 2**. For the DW images the actual b-value differs up to 2% from the applied b-value. The relative difference is largest for lower b-values. The effect of these small differences is shown in **Figure 6**, **C** and **D**, where the intensity-normalized mean signal (with and without signal-drift correction is plotted as a function of both the applied and the actual b-value. The imaging gradients not only affect the b-value, but also the gradient direction. However, the median change in orientation due to the slice selection gradients across all gradients was found to be only 0.004 degrees. The applied and actual b-matrix values can be found in the lookup table which can be downloaded from the website www.massive-data.org.

Correcting for subject motion, eddy current distortions, and EPI deformations

The average maximal translations over all individual sessions were 0.3 ± 3.3 mm (range -4.7 to 4.6 mm), 0.4 ± 1.2 mm (range -2.5 to 2.8 mm), and -0.8 ± 1.3 mm (range -3.6 to 2.3 mm) for the coronal, sagittals and axial directions, respectively. The average maximal rotations over all individual session were -0.6 ± 1.0 ° (range -2.5 to 2.9 °), 0.2 ± 1.2 ° (range -2.9 to 2.6 °), and -0.2 ± 1.1 ° (range -2.3 to 2.4 °) along the coronal (roll), sagittal (pitch), and axial (yaw) axes, respectively. The maximal range of the rotations between and within the sessions was only ±5 degrees with respect to the mean. The difference between the imposed gradient distribution and the gradient distribution after b-matrix correction for subject motion is shown for a subset of the data (b=1000 s/mm^2 and b=3000 s/mm^2 volumes) in **Supporting material 1, Figure S2**.

Figure 7 shows the differences in image distortions between AP and PA phase encoding directions, on the one hand, and positive and negative diffusion weighting gradient directions, on the other hand (AP+, AP-, PA+, PA-). The differences in the distortions between the AP and PA phase-encoding directions can be appreciated most in the regions of the eyes, the temporal lobes, and the cerebellum. The difference in distortions between positive and negative gradient directions is reflected by the opposite eddy current distortions (e.g., compressions vs. stretches along the phase-encoding orientation). The color-coded FA map (**Figure 8 A**) and the T_1-weighted data (**Figure 8 B**) in anatomical space with a 1x1x1 mm^3 voxel size are shown in **Figure 8**. The alignment of both datasets after motion correction, eddy current distortion correction, and EPI distortion correction by registration to the T_1-weighted image is illustrated in **Figure 8 C**. The registered data in the anatomical space is available with a 2.5x2.5x2.5 mm^3 (website) and a 1x1x1 mm^3 voxel size (upon request, due to limited online storage capacity).

Discussion

In this work, we have presented the MASSIVE brain dataset, which contains 8000 in vivo dMRI volumes of a healthy subject. Currently, the raw, intensity-normalized, signal-drift corrected, and subject motion / eddy current distortion / EPI distortion corrected dMRI data can be downloaded from www.massive-data.org. All the B_0 field maps, noise maps, and the volumetric FLAIR, T_1-, and T_2-weighted datasets are also made available.

We have established a platform through the MASSIVE website to share improvements of specific processing steps and updates of the processed data. Such methodological developments encompass novel subject motion and distortion correction methods, new microstructural modeling approaches, etc. Similarly, we anticipate that segmentations of the anatomical images (e.g., T_1- and T_2-weighted images) using common brain atlases and processing tools will also become available.

The purpose of MASSIVE is to serve as an extensive dataset to compare, evaluate, and validate existing or novel diffusion MRI methods, such as preprocessing steps, signal modeling, tissue characterization, and analysis strategies. While existing brain dMRI databases can provide data from many subjects with only moderate coverage of q-space, none of these provide dMRI data from a single subject with as dense a q-space sampling as provided in the MASSIVE database. MASSIVE is unique in consisting of 8000 DW volumes that are sampled on shells as well as two Cartesian grids. The data was acquired on a standard clinical system using a coil and acquisition settings that are commonly available. This makes the data quality of each individual dMRI volume comparable to data typically acquired in most clinical studies, which means that subset of the data, e.g. containing 100 dMRI volumes with $b = 1000 s/mm^2$, would closely resemble a clinical acquisition. As such, methods and models derived from this database can easily be transferred to other clinical and pre-clinical research workflows.

Examples of research questions that have already been addressed using the MASSIVE brain database include characterizing signal drift in dMRI acquisitions (16), investigating the in vivo trade-off between accuracy and precision of multi-fiber methods with respect to b-value and number of gradient orientations (80), studying the difference between interpolation methods for transforming dMRI data between grids and shells (81), and characterizing single fiber population signal profiles using a wide range of reconstruction strategies (82). Furthermore, the MASSIVE dataset could be useful in investigating the optimality of different EPI distortion correction techniques, e.g. using field maps, registration to an anatomical image, or using opposite phase encoding images. Commonly used dMRI acquisition protocols sample either the upper or lower hemisphere in q-space. However, eddy current correction techniques might benefit from sampling on the whole sphere (83). In addition to correcting for image distortions, correction for subject motion remains an active field of research in which new methods (e.g. targeted to high b-values) are constantly being developed and evaluated (84,85). Therefore, the optimal acquisition scheme to adequately correct for artifacts and motion remains an open question, and the MASSIVE dataset could be subsampled to investigate such issues. In addition, whereas there is a reasonable consensus of an 'ideal' single shell acquisition for diffusion tensor imaging (86), optimal acquisition strategies for many of the other diffusion models are still being investigated and new models are constantly under development (14,51,87–91). The MASSIVE brain database, and in particular the unique dMRI dataset, which – to the best of our knowledge – represents the largest in vivo dMRI dataset of a single subject to date, will avert the need to continuously reacquire optimized data and boost new developments in diffusion modeling and processing.

Conclusion

We have presented the MASSIVE (Multiple Acquisitions for Standardization of Structural Imaging Validation and Evaluation) brain dataset, consisting of an unprecedented set of 8000 DW volumes of a single human subject. This unique set of in vivo MRI data will provide a robust framework to evaluate novel diffusion processing techniques and to reliably compare different approaches for diffusion modeling. All data is made publicly available on *www.massive-data.org*.

Acknowledgments

SBV is funded by the National Institute for Health Research University College London Hospitals Biomedical Research Centre (NIHR BRC UCLH/UCL High Impact Initiative). CMWT is supported by a grant (No. 612.001.104) from the Physical Sciences division of the Netherlands Organisation for Scientific Research (NWO). The research of AL is supported by VIDI Grant 639.072.411 from the Netherlands Organisation for Scientific Research (NWO).

References

1. Tournier J-D, Mori S, Leemans A. Diffusion tensor imaging and beyond. Magn. Reson. Med. 2011;65:1532–1556. doi: 10.1002/mrm.22924.

2. Basser PJ, Jones DK. Diffusion-tensor MRI: Theory, experimental design and data analysis - A technical review. NMR Biomed. 2002;15:456–467. doi: 10.1002/nbm.783.

3. Assaf Y, Pasternak O. Diffusion tensor imaging (DTI)-based white matter mapping in brain research: A review. J. Mol. Neurosci. 2008;34:51–61. doi: 10.1007/s12031-007-0029-0.

4. Sundgren PC, Dong Q, G??mez-Hassan D, Mukherji SK, Maly P, Welsh R. Diffusion tensor imaging of the brain: Review of clinical applications. Neuroradiology 2004;46:339–350. doi: 10.1007/s00234-003-1114-x.

5. Tax CMW, Vos SB, Leemans A. Checking and correcting DTI data. In: Hecke W van, Emsell L, Sunaert S, editors. Diffusion Tensor Imaging A Practical Handbook. ; 2016.

6. Basser PJ, Mattiello J, LeBihan D. Estimation of the effective self-diffusion tensor from the NMR spin echo. J. Magn. Reson. B 1994;103:247–254. doi: 10.1006/jmrb.1994.1037.

7. Jensen JH, Helpern JA, Ramani A, Lu H, Kaczynski K. Diffusional kurtosis imaging: The quantification of non-Gaussian water diffusion by means of magnetic resonance imaging. Magn. Reson. Med. 2005;53:1432–1440. doi: 10.1002/mrm.20508.

8. Wedeen VJ, Hagmann P, Tseng WYI, Reese TG, Weisskoff RM. Mapping complex tissue architecture with diffusion spectrum magnetic resonance imaging. Magn. Reson. Med. 2005;54:1377–1386. doi: 10.1002/mrm.20642.

9. Tuch DS. Q-ball imaging. Magn. Reson. Med. 2004;52:1358–1372. doi: 10.1002/mrm.20279.

10. Tournier JD, Calamante F, Connelly A. Robust determination of the fibre orientation distribution in diffusion MRI: Non-negativity constrained super-resolved spherical deconvolution. Neuroimage 2007;35:1459–1472. doi: 10.1016/j.neuroimage.2007.02.016.

11. Dell'Acqua F, Rizzo G, Scifo P, Clarke RA, Scotti G, Fazio F. A Model-Based Deconvolution Approach to Solve °Fiber Crossing in Diffusion-Weighted MR Imaging. Biomed. Eng. {IEEE} Trans. 2007;54:462--472.

12. Dell'Acqua F, Scifo P, Rizzo G, Catani M, Simmons A, Scotti G, Fazio F. A modified damped Richardson-Lucy algorithm to reduce isotropic background effects in spherical deconvolution. Neuroimage 2010;49:1446–1458. doi: 10.1016/j.neuroimage.2009.09.033.

13. Assaf Y, Basser PJ. Composite hindered and restricted model of diffusion (CHARMED) MR imaging of the human brain. Neuroimage 2005;27:48–58. doi: 10.1016/j.neuroimage.2005.03.042.

14. Zhang H, Schneider T, Wheeler-Kingshott CA, Alexander DC. NODDI: Practical in vivo neurite orientation dispersion and density imaging of the human brain. Neuroimage 2012;61:1000–1016. doi: 10.1016/j.neuroimage.2012.03.072.

15. Perrone D, Aelterman J, Pi??urica A, Jeurissen B, Philips W, Leemans A. The effect of Gibbs ringing artifacts on measures derived from diffusion MRI. Neuroimage 2015;120:441–455. doi: 10.1016/j.neuroimage.2015.06.068.

16. Vos SB, Tax CMW, Luijten PR, Ourselin S, Leemans A, Froeling M. The Importance of Correcting for Signal Drift in Diffusion MRI. Magn. Reson. Med. 2016;00:1–15. doi: 10.1002/mrm.26124.

17. Bach M, Fritzsche KH, Stieltjes B, Laun FB. Investigation of resolution effects using a specialized diffusion tensor phantom. Magn. Reson. Med. 2014;71:1108–1116. doi: 10.1002/mrm.24774.

18. Close TG, Tournier JD, Calamante F, Johnston LA, Mareels I, Connelly A. A software tool to generate simulated white matter structures for the assessment of fibre-tracking algorithms. Neuroimage 2009;47:1288–1300. doi: 10.1016/j.neuroimage.2009.03.077.

19. Leemans A, Sijbers J, Verhoye M, Van Der Linden A, Van Dyck D. Mathematical framework for simulating diffusion tensor MR neural fiber bundles. Magn. Reson. Med. 2005;53:944–953. doi: 10.1002/mrm.20418.

20. Neher PF, Laun FB, Stieltjes B, Maier-Hein KH. Fiberfox: Facilitating the creation of realistic white matter software phantoms. Magn. Reson. Med. 2014;72:1460–1470. doi: 10.1002/mrm.25045.

21. Eickhoff S, Nichols TE, Van Horn JD, Turner JA. Sharing the wealth: Neuroimaging data repositories. Neuroimage 2016;124:1065–1068. doi: 10.1016/j.neuroimage.2015.10.079.

22. Walker L, Chang L-C, Nayak A, et al. The diffusion tensor imaging (DTI) component of the NIH MRI study of normal brain development (PedsDTI). Neuroimage 2016;124:1125–1130. doi: 10.1016/j.neuroimage.2015.05.083.

23. Karayanidis F, Keuken MC, Wong A, et al. The Age-ility Project (Phase 1): Structural and functional imaging and electrophysiological data repository. Neuroimage 2015;124:1137–1142. doi: 10.1016/j.neuroimage.2015.04.047.

24. Evans AC. The NIH MRI study of normal brain development. Neuroimage 2006;30:184–202. doi: 10.1016/j.neuroimage.2005.09.068.

25. Van Essen DC, Smith SM, Barch DM, Behrens TEJ, Yacoub E, Ugurbil K. The WU-Minn Human Connectome Project: An overview. Neuroimage 2013;80:62–79. doi: 10.1016/j.neuroimage.2013.05.041.

26. Hodge MR, Horton W, Brown T, et al. ConnectomeDB-Sharing human brain connectivity data. Neuroimage 2016;124:1102–1107. doi: 10.1016/j.neuroimage.2015.04.046.

27. Hsu Y-C, Lo Y-C, Chen Y-J, Wedeen VJ, Isaac Tseng W-Y. NTU-DSI-122: A diffusion spectrum imaging template with high anatomical matching to the ICBM-152 space. Hum. Brain Mapp. 2015;36:3528–3541. doi: 10.1002/hbm.22860.

28. Zhang S, Peng H, Dawe RJ, Arfanakis K. Enhanced ICBM diffusion tensor template of the human brain. Neuroimage 2011;54:974–984. doi: 10.1016/j.neuroimage.2010.09.008.

29. Varentsova A, Zhang S, Arfanakis K. Development of a high angular resolution diffusion imaging human brain template. Neuroimage 2014;91:177–186. doi: 10.1016/j.neuroimage.2014.01.009.

30. Mori S, Wakana S, Lidia, van Zijl P. MRI Atlas of Human White Matter. Academic Press; 2005. doi: 10.1016/B978-008043924-2/50055-9.

31. Calabrese E, Badea A, Coe CL, Lubach GR, Shi Y, Styner MA, Johnson GA. A diffusion tensor MRI atlas of the postmortem rhesus macaque brain. Neuroimage 2015;117:408–416. doi: 10.1016/j.neuroimage.2015.05.072.

32. Dyrby TB, Baaré WFC, Alexander DC, Jelsing J, Garde E, Søgaard L V. An ex vivo imaging pipeline for producing high-quality and high-resolution diffusion-weighted imaging datasets. Hum. Brain Mapp. 2011;32:544–563. doi: 10.1002/hbm.21043.

33. Calabrese E, Hickey P, Hulette C, Zhang J, Parente B, Lad SP, Johnson GA. Postmortem diffusion MRI of the human brainstem and thalamus for deep brain stimulator electrode localization. Hum. Brain Mapp. 2015;3178:3167–3178. doi: 10.1002/hbm.22836.

34. Fan Q, Witzel T, Nummenmaa A, et al. MGH-USC Human Connectome Project datasets with ultra-high b-value diffusion MRI. Neuroimage 2016;124:1108–1114. doi: 10.1016/j.neuroimage.2015.08.075.

35. Poldrack RA, Laumann TO, Koyejo O, et al. Long-term neural and physiological phenotyping of a single human. Nat. Commun. 2015;6:8885. doi: 10.1038/ncomms9885.

36. Tax CMW, Jeurissen B, Vos SB, Viergever MA, Leemans A. Recursive calibration of the fiber response function for spherical deconvolution of diffusion MRI data. Neuroimage 2014;86:67–80. doi: 10.1016/j.neuroimage.2013.07.067.

37. Vos SB, Viergever MA, Leemans A. Multi-fiber tractography visualizations for diffusion MRI data. PLoS One 2013;8:1–17. doi: 10.1371/journal.pone.0081453.

38. Fillard P, Descoteaux M, Goh A, et al. Quantitative evaluation of 10 tractography algorithms on a realistic diffusion MR phantom. Neuroimage 2011;56:220–234. doi: 10.1016/j.neuroimage.2011.01.032.

39. Poupon C, Rieul B, Kezele I, Perrin M, Poupon F, Mangin JF. New diffusion phantoms dedicated to the study and validation of high-angular-resolution diffusion imaging (HARDI) models. Magn. Reson. Med. 2008;60:1276–1283. doi: 10.1002/mrm.21789.

40. Pujol S, Wells W, Pierpaoli C, et al. The DTI Challenge: Toward Standardized Evaluation of Diffusion Tensor Imaging Tractography for Neurosurgery. J. Neuroimaging 2015;25:875–882. doi: 10.1111/jon.12283.

41. Huang H, Ceritoglu C, Li X, Qiu A, Miller MI, van Zijl PCM, Mori S. Correction of B0 susceptibility induced distortion in diffusion-weighted images using large-deformation diffeomorphic metric mapping. Magn. Reson. Imaging 2008;26:1294–1302. doi: 10.1016/j.mri.2008.03.005.

42. Irfanoglu MO, Walker L, Sarlls J, Marenco S, Pierpaoli C. Effects of image distortions originating from susceptibility variations and concomitant fields on diffusion MRI tractography results. Neuroimage 2012;61:275–288. doi: 10.1016/j.neuroimage.2012.02.054.

43. Smith RE, Tournier JD, Calamante F, Connelly A. SIFT: Spherical-deconvolution informed filtering of tractograms. Neuroimage 2013;67:298–312. doi: 10.1016/j.neuroimage.2012.11.049.

44. Duning T, Kloska S, Steinsträter O, Kugel H, Heindel W, Knecht S. Dehydration confounds the assessment of brain atrophy. Neurology 2005;64:548–550. doi: 10.1212/01.WNL.0000150542.16969.CC.

45. Maclaren J, Han Z, Vos SB, Fischbein N, Bammer R. Reliability of brain volume measurements: A test-retest dataset. Sci. Data 2014;1:140037. doi: 10.1038/sdata.2014.37.

46. de Bresser J, Portegies MP, Leemans A, Biessels GJ, Kappelle LJ, Viergever MA. A comparison of MR based segmentation methods for measuring brain atrophy progression. Neuroimage 2011;54:760–768. doi: 10.1016/j.neuroimage.2010.09.060.

47. Froeling M, Tax CMW, Vos SB, Luijten PR, Leemans A. MASSIVE: Multiple Acquisitions for Standardization of Structural Imaging Validation and Evaluation. In: 22th Scientific Meeting of the International Society for Magnetic Resonance in Medicine. Vol. 27. Milan; 2014. p. 2582.

48. Andersson JLR, Skare S, Ashburner J. How to correct susceptibility distortions in spin-echo echo-planar images: Application to diffusion tensor imaging. Neuroimage 2003;20:870–888. doi: 10.1016/S1053-8119(03)00336-7.

49. Ruthotto L, Kugel H, Olesch J, Fischer B, Modersitzki J, Burger M, Wolters CH. Diffeomorphic susceptibility artifact correction of diffusion-weighted magnetic resonance images. Phys. Med. Biol. 2012;57:5715–5731. doi: 10.1088/0031-9155/57/18/5715.

50. Jezzard P, Balaban RS. Correction for geometric distortion in echo planar images from B(o) field variations. Magn. Reson. Med. 1995;34:65–73. doi: 10.1002/mrm.1910340111.

51. Caruyer E, Lenglet C, Sapiro G, Deriche R. Design of multishell sampling schemes with uniform coverage in diffusion MRI. Magn. Reson. Med. 2013;69:1534–40. doi: 10.1002/mrm.24736.

52. Jones DK, Horsfield MA, Simmons A. Optimal strategies for measuring diffusion in anisotropic systems by magnetic resonance imaging. Magn. Reson. Med. 1999;42:515–525. doi: 10.1002/(SICI)1522-2594(199909)42:3<515::AID-MRM14>3.0.CO;2-Q.

53. Cook PA, Symms M, Boulby PA, Alexander DC. Optimal acquisition orders of diffusion-weighted MRI measurements. J. Magn. Reson. Imaging 2007;25:1051–1058. doi: 10.1002/jmri.20905.

54. Kleinnijenhuis M, Barth M, Alexander DC, van Cappellen van Walsum AM, Norris DG. Structure Tensor Informed Fiber Tractography (STIFT) by combining gradient echo MRI and diffusion weighted imaging. Neuroimage 2012;59:3941–3954. doi: 10.1016/j.neuroimage.2011.10.078.

55. Concha L, Gross DW, Beaulieu C. Diffusion tensor tractography of the limbic system. AJNR. Am. J. Neuroradiol. 2005;26:2267–2274.

56. Metzler-Baddeley C, O'Sullivan MJ, Bells S, Pasternak O, Jones DK. How and how not to correct for CSF-contamination in diffusion MRI. Neuroimage 2012;59:1394–1403. doi: 10.1016/j.neuroimage.2011.08.043.

57. Farrell JAD, Landman BA, Jones CK, Smith SA, Prince JL, Van Zijl PCM, Mori S. Effects of signal-to-noise ratio on the accuracy and reproducibility of diffusion tensor imaging-derived fractional anisotropy, mean diffusivity, and principal eigenvector measurements at 1.5T. J. Magn. Reson. Imaging 2007;26:756–767. doi: 10.1002/jmri.21053.

58. Landman BA, Farrell JAD, Jones CK, Smith SA, Prince JL, Mori S. Effects of diffusion weighting schemes on the reproducibility of DTI-derived fractional anisotropy, mean diffusivity, and principal eigenvector measurements at 1.5T. Neuroimage 2007;36:1123–1138. doi: 10.1016/j.neuroimage.2007.02.056.

59. Jones DK. The Effect of Gradient Sampling Schemes on Measures Derived from Diffusion Tensor MRI: A Monte Carlo Study. Magn. Reson. Med. 2004;51:807–815. doi: 10.1002/mrm.20033.

60. Anderson AW. Theoretical analysis of the effects of noise on diffusion tensor imaging. Magn. Reson. Med. 2001;46:1174–1188. doi: 10.1002/mrm.1315 [pii].

61. Jones DK. Determining and visualizing uncertainty in estimates of fiber orientation from diffusion tensor MRI. Magn. Reson. Med. 2003;49:7–12. doi: 10.1002/mrm.10331.

62. Lu H, Jensen JH, Ramani A, Helpern JA. Three-dimensional characterization of non-gaussian water diffusion in humans using diffusion kurtosis imaging. NMR Biomed. 2006;19:236–247. doi: 10.1002/nbm.1020.

63. Veraart J, Rajan J, Peeters RR, Leemans A, Sunaert S, Sijbers J. Comprehensive framework for accurate diffusion MRI parameter estimation. Magn. Reson. Med. 2013;70:972–984. doi: 10.1002/mrm.24529.

64. Veraart J, Sijbers J, Sunaert S, Leemans A, Jeurissen B. Weighted linear least squares estimation of diffusion MRI parameters: Strengths, limitations, and pitfalls. Neuroimage 2013;81:335–346. doi: 10.1016/j.neuroimage.2013.05.028.

65. Kaufman L, Kramer DM, Crooks LE, Ortendahl D a. Measuring signal-to-noise ratios in MR imaging. Radiology 1989;173:265–267. doi: 10.1148/radiology.173.1.2781018.

66. Firbank MJ, Coulthard A, Harrison RM, Williams ED. A comparison of two methods for measuring

the signal to noise ratio on MR images. Phys Med Biol 1999;44:N261–4.

67. Dietrich O, Raya JG, Reeder SB, Reiser MF, Schoenberg SO. Measurement of signal-to-noise ratios in MR images: Influence of multichannel coils, parallel imaging, and reconstruction filters. J. Magn. Reson. Imaging 2007;26:375–385. doi: 10.1002/jmri.20969.

68. Reeder SB, Wintersperger BJ, Dietrich O, Lanz T, Greiser A, Reiser MF, Glazer GM, Schoenberg SO. Practical approaches to the evaluation of signal-to-noise ratio performance with parallel imaging: Application with cardiac imaging and a 32-channel cardiac coil. Magn. Reson. Med. 2005;54:748–754. doi: 10.1002/mrm.20636.

69. Polders DL, Leemans A, Hendrikse J, Donahue MJ, Luijten PR, Hoogduin JM. Signal to noise ratio and uncertainty in diffusion tensor imaging at 1.5, 3.0, and 7.0 Tesla. J. Magn. Reson. Imaging 2011;33:1456–1463. doi: 10.1002/jmri.22554.

70. Jeurissen B, Leemans A, Tournier JD, Jones DK, Sijbers J. Investigating the prevalence of complex fiber configurations in white matter tissue with diffusion magnetic resonance imaging. Hum. Brain Mapp. 2013;34:2747–2766. doi: 10.1002/hbm.22099.

71. Mattiello J, Basser PJ, Le Bihan D. The b matrix in diffusion tensor echo-planar imaging. Magn. Reson. Med. 1997;37:292–300. doi: 10.1002/mrm.1910370226.

72. Mattiello J, Basser PJ, Lebihan D. Analytical Expressions for the B-Matrix in Nmr Diffusion Imaging and Spectroscopy. J. Magn. Reson. Ser. A 1994;108:131–141.

73. Jones DK, Cercignani M. Twenty-five pitfalls in the analysis of diffusion MRI data. NMR Biomed. 2010;23:803–820. doi: 10.1002/nbm.1543.

74. Leemans A, Jones DK. The B-matrix must be rotated when correcting for subject motion in DTI data. Magn. Reson. Med. 2009;61:1336–1349. doi: 10.1002/mrm.21890.

75. Leemans A, Jeurissen B, Sijbers J, Jones D. ExploreDTI: a graphical toolbox for processing, analyzing, and visualizing diffusion MR data. In: Proceedings 17th Scientific Meeting, International Society for Magnetic Resonance in Medicine. Vol. 17. Honolulu; 2009. p. 3537.

76. Rohde GK, Barnett AS, Basser PJ, Marenco S, Pierpaoli C. Comprehensive Approach for Correction of Motion and Distortion in Diffusion-Weighted MRI. Magn. Reson. Med. 2004;51:103–114. doi: 10.1002/mrm.10677.

77. Wu M, Chang LC, Walker L, Lemaitre H, Barnett a S, Marenco S, Pierpaoli C. Comparison of EPI distortion correction methods in diffusion tensor MRI using a novel framework. Med. Image Comput. Comput. Assist. Interv. 2008;11:321–329. doi: 10.1007/978-3-540-85990-1-39.

78. Irfanoglu MO, Walker L, Sammet S, Pierpaoli C, Machiraju R. Susceptibility distortion correction for echo planar images with non-uniform B-spline grid sampling: A diffusion tensor image study. Lect. Notes Comput. Sci. (including Subser. Lect. Notes Artif. Intell. Lect. Notes Bioinformatics) 2011;6892 LNCS:174–181. doi: 10.1007/978-3-642-23629-7_22.

79. Vos SB, Aksoy M, Han Z, Holdsworth SJ, Viergever MA, Leemans A, Bammer R. Trade-off between angular and spatial resolution in in vivo fiber tractography. Neuroimage 2016;129:117–132. doi: 10.1016/j.neuroimage.2016.01.011.

80. Vos SB, Tax CMW, Froeling M, Leemans A. In vivo investigations of accuracy and precision of fiber orientations in crossing fibers in spherical deconvolution-based HARDI methods. In: Proceedings 22nd Scientific Meeting, International Society for Magnetic Resonance in Medicine. Vol. 22. ; 2014. p. 976.

81. Tax CMW, Vos SB, Viergever MA, Froeling M, Leemans A. Transforming Grids To Shells and Vice Versa : an Evaluation of Interpolation Methods in Diffusion MRI q- and b-space. In: Proceedings 22nd

Scientific Meeting, International Society for Magnetic Resonance in Medicine. Vol. 22. ; 2014. p. 4485.

82. Tax CMW, Novikov DS, Garyfallidis E, Viergever MA, Descoteaux M, Leemans A. Localizing and Characterizing Single Fiber Populations Throughout the Brain. In: Proceedings 23nd Scientific Meeting, International Society for Magnetic Resonance in Medicine. ; 2015. p. 0473.

83. Andersson JLR, Sotiropoulos SN. An integrated approach to correction for off-resonance effects and subject movement in diffusion MR imaging. Neuroimage 2015;125:1063–1078. doi: 10.1016/j.neuroimage.2015.10.019.

84. Ben-Amitay S, Jones DK, Assaf Y. Motion correction and registration of high b-value diffusion weighted images. Magn. Reson. Med. 2012;67:1694–1702. doi: 10.1002/mrm.23186.

85. Huizinga W, Poot DHJ, Guyader J-M, et al. PCA-based groupwise image registration for quantitative MRI. Med. Image Anal. 2015;29:65–78. doi: 10.1016/j.media.2015.12.004.

86. Jones DK, Leemans A. Diffusion tensor imaging. Meth Molec Biol 2011;711:127–44. doi: 10.1007/978-1-61737-992-5_6.

87. De Santis S, Assaf Y, Evans CJ, Jones DK. Improved precision in CHARMED assessment of white matter through sampling scheme optimization and model parsimony testing. Magn. Reson. Med. 2014;71:661–671. doi: 10.1002/mrm.24717.

88. Kuo LW, Chen JH, Wedeen VJ, Tseng WYI. Optimization of diffusion spectrum imaging and q-ball imaging on clinical MRI system. Neuroimage 2008;41:7–18. doi: 10.1016/j.neuroimage.2008.02.016.

89. Hoy AR, Kecskemeti SR, Alexander AL. Free water elimination diffusion tractography: A comparison with conventional and fluid-attenuated inversion recovery, diffusion tensor imaging acquisitions. J. Magn. Reson. Imaging 2015:n/a–n/a. doi: 10.1002/jmri.24925.

90. Jelescu IO, Zurek M, Winters K V., et al. In vivo quantification of demyelination and recovery using compartment-specific diffusion MRI metrics validated by electron microscopy. Neuroimage 2016. doi: 10.1016/j.neuroimage.2016.02.004.

91. Jensen JH, Russell Glenn G, Helpern JA. Fiber ball imaging. Neuroimage 2016;124:824–833. doi: 10.1016/j.neuroimage.2015.09.049.

Figure Captions

Figure 1: Schematic overview of the MRI acquisition protocol of a single session.

Figure 2: Schematic representation of the encoding schemes in q-space. **A)** The 5 shells (b= 500, 1000, 2000, 3000 and 4000 s/mm^2). **B)** The two Cartesian DSI grids (DSI8: light gray, DSI9 dark gray). **C)** The five shells and the two Cartesian grids combined. **D-E)** Examples of the random selection of gradients for each session. The gradients defined along the positive direction are shown in color, whereas the mirrored gradient directions are shown in light gray. All the gradients are color-coded for their session. **F)** The 18 sessions combined fill up half of the q-space (2000 orientations) and by mirroring the gradients the q-space is fully filled.

Figure 3: Representative images of the acquired data (intensity windowing is adjusted for each image). Diffusion-weighted images with an applied b-value of: **A)** 0 s/mm^2, **B)** 500 s/mm^2, **C)** 1000 s/mm^2, **D)** 2000 s/mm^2, **E)** 3000 s/mm^2, **F)** 4000 s/mm^2, **G)** 5500 s/mm^2, **H)** 9000 s/mm^2. Anatomical images: **I)** T_1–weighted image, **J)** T_2–weighted image, and **K)** FLAIR. **L)** B_0 phase map.

Figure 4: Method and result used for SNR calculation. **A)** Schematic representation of the method used for SNR calculation. Using a whole-brain mask the average signal was estimated from the diffusion weighted volume. The noise standard deviation was estimated using the acquired noise map in which the noise is Rayleigh distributed as shown in the probability density histogram. **B)** Estimated SNR using the acquired noise map. Black markers are for session 1 to 8 ($b \leq 3000$ s/mm^2) and blue markers are for session 9 to 18 ($b > 3000$ s/mm^2 and DSI grids). The left image shows the SNR per session in the scanned order, the middle image shows the SNR per session sorted for the SNR, and the right image shows the SNR for all the volumes. The SNR levels of the different shells can clearly be identified.

Figure 5: Original (red) and signal-drift corrected (blue) average signal of the non-diffusion-weighted volumes for 24 acquisition blocks of 15 minutes. The black line describes the quadratic signal drift (see Eq. 1) and the dashed line is the theoretically constant signal of 100%.

Figure 6: A-B) The mean signal per acquired volume of the drift-uncorrected volumes (top row - **A**) signal-drift corrected volumes (bottom row - **B**). The left column shows the signal per session in the scanned order, the middle column shows the mean signal for all sessions in the scanned order and the right column shows the signal for all the volumes sorted for the signal values. **C-D)** The intensity-normalized mean signal per acquired volume as a function of the b-value for all 8000 volumes (top row) and a zoomed b-value range (bottom row). The signal is plotted using a linear and a logarithmic scaling of the y-axes revealing the obvious non-exponential decay of the diffusion weighted signal. **C)** The normalized mean signal (but not corrected for signal drift) as a function of the predefined b-value. **D)** The intensity-normalized and signal-drift corrected mean signal as function of the actual b-value. The bottom row clearly shows how the "effective" b-value causes a spread of the signal over the b-value axes, that correctly follows the signal decay.

Figure 7: Representative images for the different phase encoding (AP+, AP-, PA+, PA-) directions. Axial (**A** and **C**) and sagittal (**B** and **D**) cross-sectional images of a non-diffusion-weighted (**A** and **B**, b = 0 s/mm^2) and a diffusion-weighted (**C** and **D,** b = 1000 s/mm^2) volume with the different phase encoding directions and gradient signs. The differences in the distortions between the AP and PA phase encoding directions can be appreciated most in the eyes (green arrows), temporal region (blue arrows), and the cerebellum (red arrows).

Figure 8: Example DTI reconstruction of the MASSIVE data**. A)** Color coded FA maps after applying all the correction procedures. **B)** T_1 weighted data, which were used here to correct for EPI deformations. **C)** Color coded FA maps fused with T_1 weighted data to appreciate the quality of the processing.

Figure S-1: A) Iterative method of optimization, first all particles are repulsed (red) after which they are projected back on the unit sphere (blue). The resulting particles (green) are then used for the next iteration. **B)** The percent change in entropy of the system over 1500 iterations for single- and multi-shell optimizations. **C)** Time it takes to perform 1000 iterations (Intel Core i5-2520M CPU, 2.5GHz) for shell ranging from 3 to 180 gradient orientations.

Figure S-2: Effect of subject motion on the imposed gradient orientations. The 500 gradient direction for b = 1000 s/mm^2 and b = 3000 s/mm2 as they were defined (**A** and **B**) and after registration with b-matrix correction (74) (**C** and **D**). The condition number of the b = 1000 s/mm^2 and b = 3000 s/mm^2 shells (1.5813 for both) changed to 1.5826 and 1.5861, respectively.

Tables

Table 1: Overview of the acquisition parameters. (Abbreviations: IR – inversion recovery, TSE – turbo spin echo, TFE – turbo field echo, SE – spin echo, EPI – echo planar imaging, FFE – fast field echo, FOV – field of view, AP – anterior posterior, RL – right left, IS – inferior superior, SENSE – sensitivity encoding, SPIR – spectral pre-saturation by inversion recovery, BW – bandwidth, NSA – number of signal averages, G – gradient strength, DSI – diffusion spectrum imaging)

	FLAIR	**T_1**	**T_2**	**DWI**	**B_0**
Sequence	3D-IR-TSE	3D-TFE	3D-TSE	2D-SE-EPI	Dual echo 2D-FFE
FOV [mm^3 / mm^2] (AP/RL/IS)	240x180x140	240x180x140	240x180x140	240x240	240x240
Acquisition matrix	240x90x140	240x90x140	240x90x140	96x96	96x96
Reconstruction matrix	240x180x140	240x180x140	240x180x140	96x96	96x96
Slice thickness [mm]	-	-	-	2.5	2.5
Voxel size [mm^3]	1x1x1	1x1x1	1x1x1	2.5x2.5x2.5	2.5x2.5x2.5
Slices	-	-	-	56	56
SENSE: AP/RL:	2/2	2/2	2/2	2.5 (AP)	-
Flip angle [°]	90	8	90	90	20
Partial Fourier	-	-	-	1 / 0.77 *	
TSE/TFE/EPI factor	182	122	124	36 (24ms) / 31 (25ms) *	-
Startup echo's	6	4	6	-	-
TE [ms]	Effective: 300 Equivalent: 128	1.25	Effective: 213 Equivalent: 92	100	First: 2 Second: 4
TR [ms]	4800	8000	2500	7000 / 7500 *	322
TI [ms]	1650	-	-	-	-
Fat suppression	SPIR	none	SPIR	SPIR	none
BW frequency [Hz]	1111	191	1111	3035/1991 *	2804
BW EPI [Hz]	-	-	-	50/30 *	-
NSA	2	1	2	1	1
Δ/δ/ζ [ms]	-	-	-	51.6 / 32.8 / 0.9	-
G_{max} [mT/m]	-	-	-	61.7	-
G_D [mT/m] (Diffusion-weighting gradient strength along one gradient axis)	-	-	-	12.6 (b500) / 17.8 (b1000) / 25.2 (b2000) / 30.9 (b3000) / 35.6 (b4000) / 27.0 (DSI8) / 30.9 (DSI9)	-
Scan time [min:s]	3:45	3:46	2:47	14:08 / 13:10 *	0:32

** Settings for session 1-8 and ($b \leq 3000$ s/mm^2) and for session 9 to 18 ($b > 3000$ s/mm^2 and DSI grids) respectively.*

Table 2: Mean values and range of the actual b-values for the 5 acquired shells.

Applied b-value in units s/mm²	Actual b-value (mean ± SD) in units s/mm²	Actual b-value range in units s/mm²	Percent deviation from applied b-value
500	500.3 ± 5.2	491.3 – 509.2	± 1.8
1000	1000.3 ± 7.3	987.6 – 1013.0	± 1.3
2000	2000.3 ± 10.4	1982.3 – 2018.2	± 0.9
3000	3000.3 ± 12.7	2978.3 – 3022.3	± 0.7
4000	4000.2 ± 15.1	3974.1 – 4026.4	± 0.7

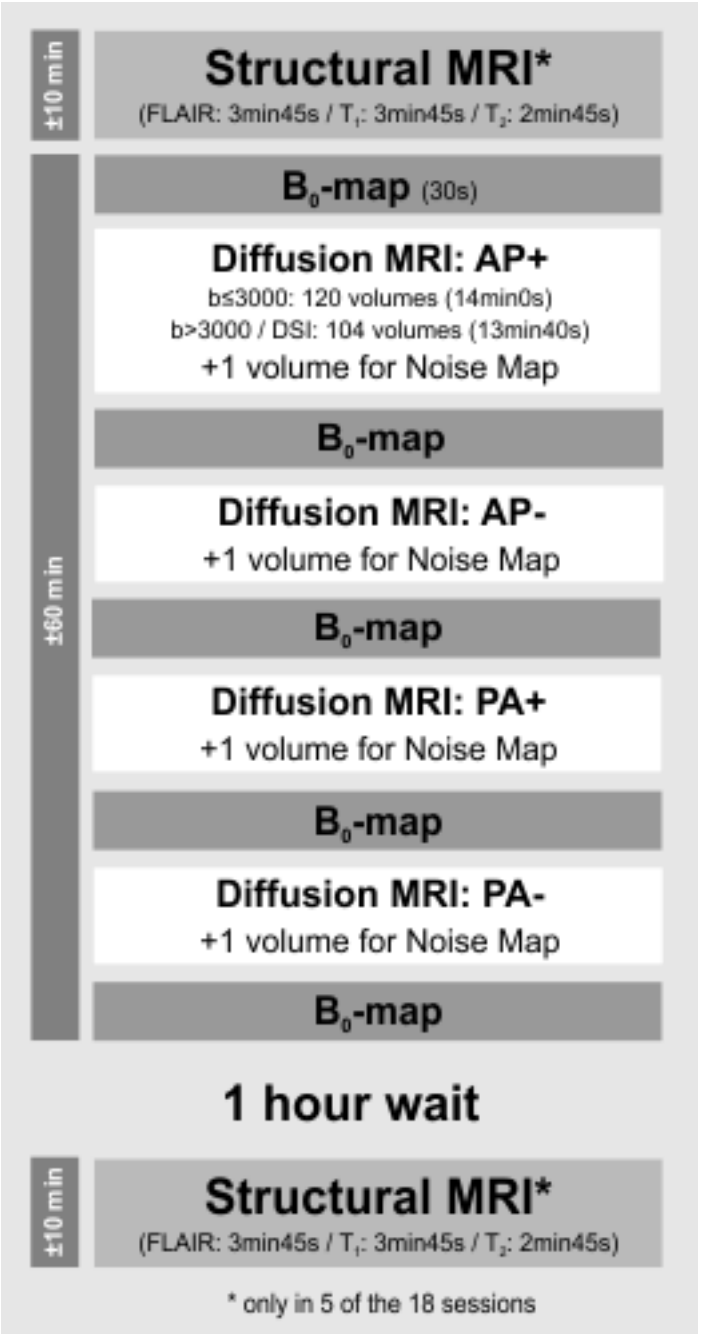

Figure 1: Schematic overview of the MRI acquisition protocol of a single session.

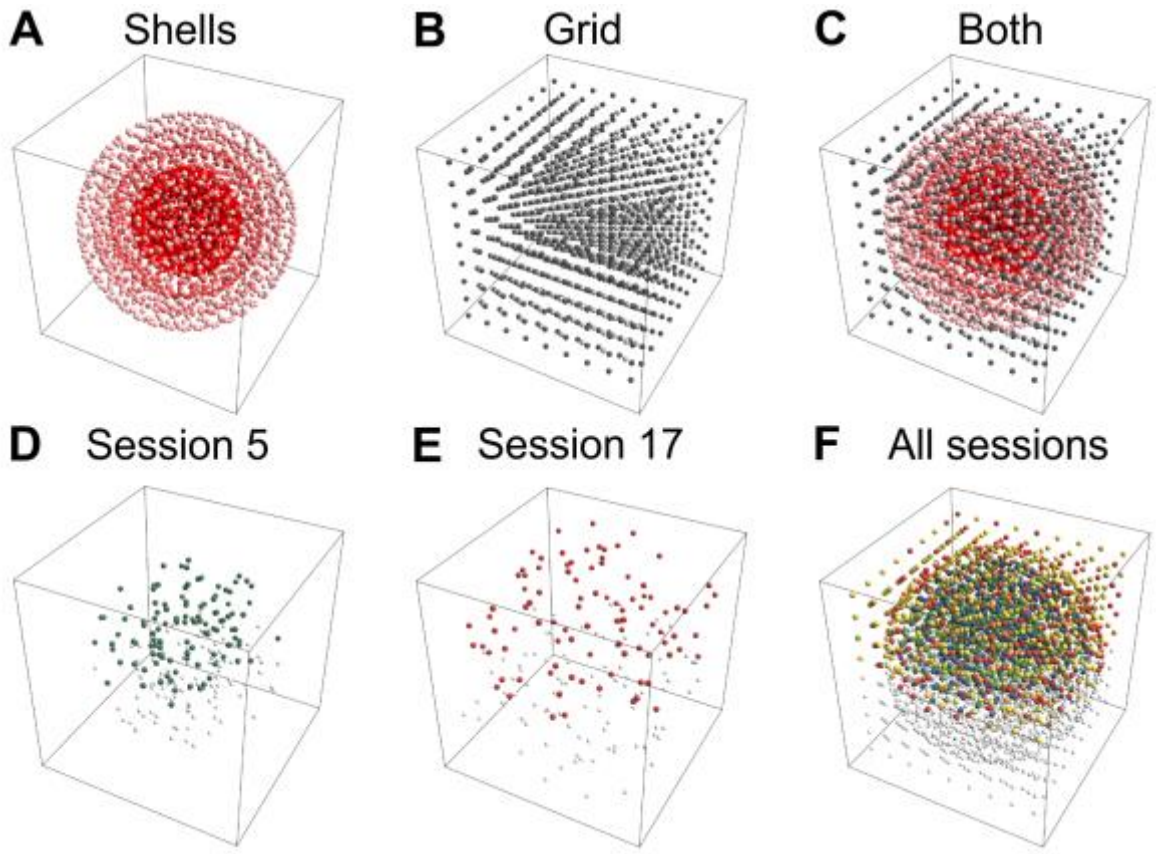

Figure 2: Schematic representation of the encoding schemes in q-space. A) The 5 shells (b= 500, 1000, 2000, 3000 and 4000 s/mm2). B) The two Cartesian DSI grids (DSI8: light gray, DSI9 dark gray). C) The five shells and the two Cartesian grids combined. D-E) Examples of the random selection of gradients for each session. The gradients defined along the positive direction are shown in color, whereas the mirrored gradient directions are shown in light gray. All the gradients are color-coded for their session. F) The 18 sessions combined fill up half of the q-space (2000 orientations) and by mirroring the gradients the q-space is fully filled.

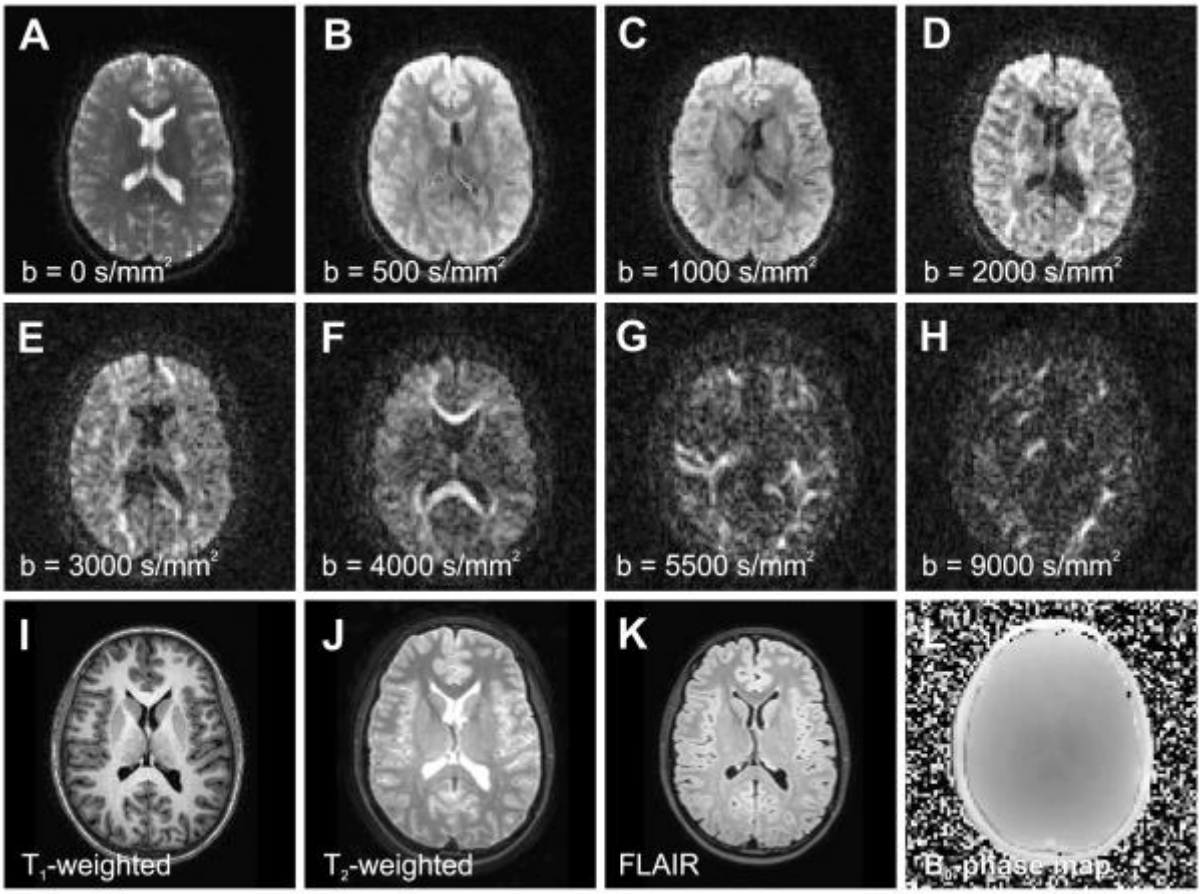

Figure 3: Representative images of the acquired data (intensity windowing is adjusted for each image). Diffusion-weighted images with an applied b-value of: A) 0 s/mm2, B) 500 s/mm2, C) 1000 s/mm2, D) 2000 s/mm2, E) 3000 s/mm2, F) 4000 s/mm2, G) 5500 s/mm2, H) 9000 s/mm2. Anatomical images: I) T1–weighted image, J) T2–weighted image , and K) FLAIR. L) B0 phase map.

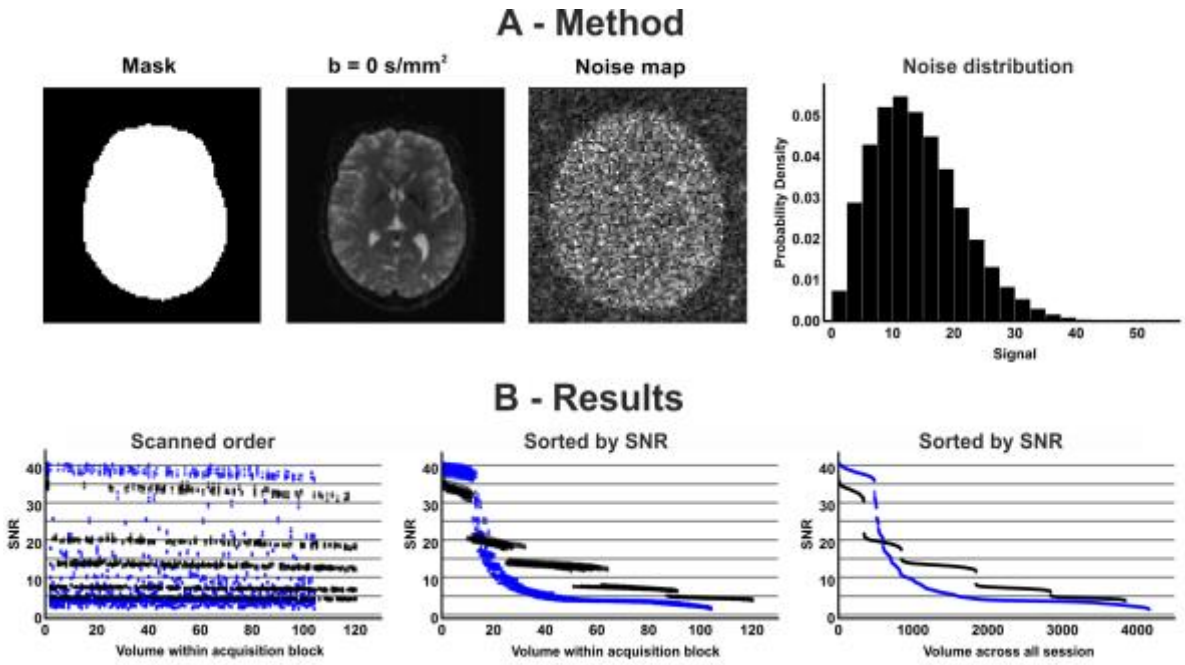

Figure 4: Method and result used for SNR calculation. A) Schematic representation of the method used for SNR calculation. Using a whole-brain mask the average signal was estimated from the diffusion weighted volume. The noise standard deviation was estimated using the acquired noise map in which the noise is Rayleigh distributed as shown in the probability density histogram. B) Estimated SNR using the acquired noise map. Black markers are for session 1 to 8 ($b \leq 3000$ s/mm2) and blue markers are for session 9 to 18 ($b > 3000$ s/mm2 and DSI grids). The left image shows the SNR per session in the scanned order, the middle image shows the SNR per session sorted for the SNR, and the right image shows the SNR for all the volumes. The SNR levels of the different shells can clearly be identified.

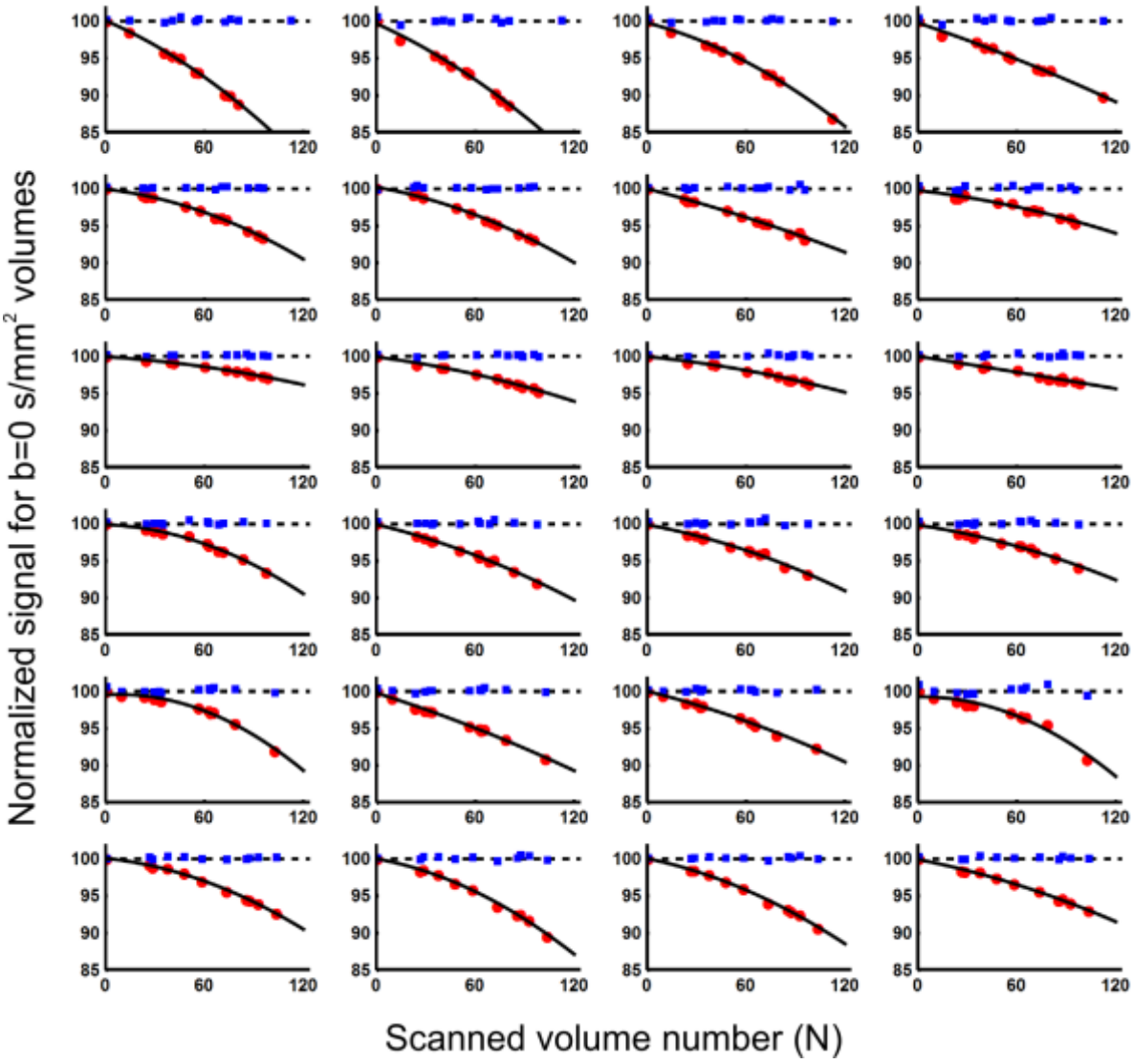

Figure 5: Original (red) and signal-drift corrected (blue) average signal of the non-diffusion-weighted volumes for 24 acquisition blocks of 15 minutes. The black line describes the quadratic signal drift (see Eq. 1) and the dashed line is the theoretically constant signal of 100%.

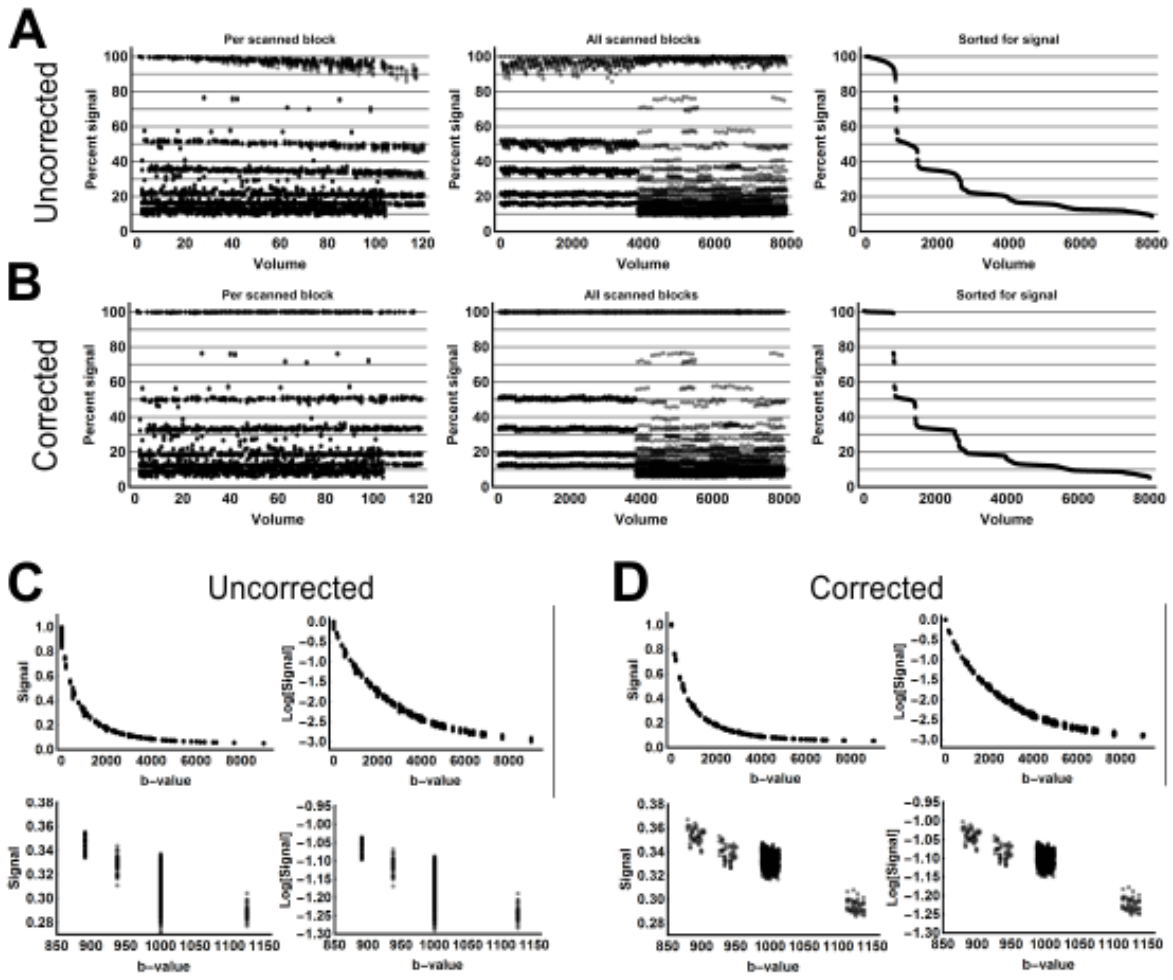

Figure 6: A-B) The mean signal per acquired volume of the drift-uncorrected volumes (top row - A) signal-drift corrected volumes (bottom row - B). The left column shows the signal per session in the scanned order, the middle column shows the mean signal for all sessions in the scanned order and the right column shows the signal for all the volumes sorted for the signal values. C-D) The intensity-normalized mean signal per acquired volume as a function of the b-value for all 8000 volumes (top row) and a zoomed b-value range (bottom row). The signal is plotted using a linear and a logarithmic scaling of the y-axes revealing the obvious non-exponential decay of the diffusion weighted signal. C) The normalized mean signal (but not corrected for signal drift) as a function of the predefined b-value. D) The intensity-normalized and signal-drift corrected mean signal as function of the actual b-value. The bottom row clearly shows how the "effective" b-value causes a spread of the signal over the b-value axes, that correctly follows the signal decay.

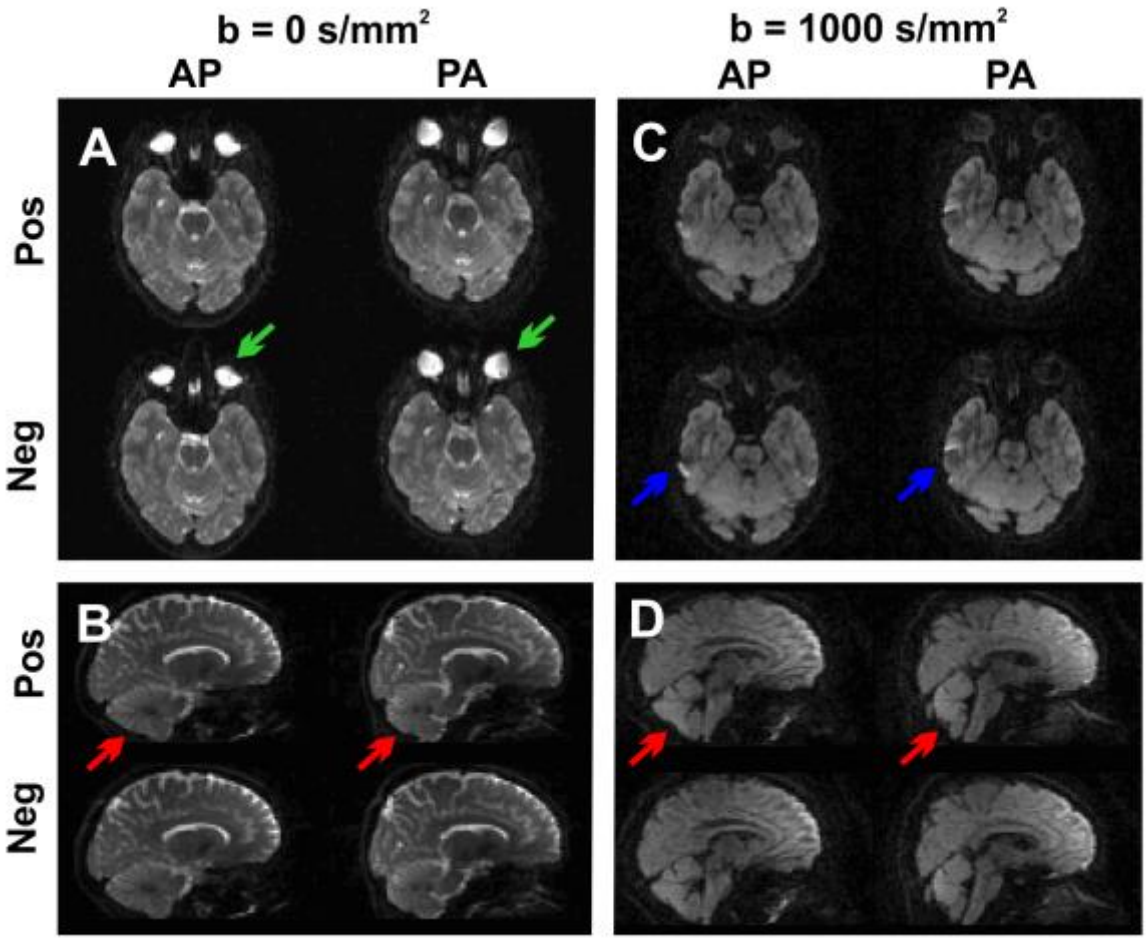

Figure 7: Representative images for the different phase encoding (AP+, AP-, PA+, PA-) directions. Axial (A and C) and sagittal (B and D) cross-sectional images of a non-diffusion-weighted (A and B, b = 0 s/mm2) and a diffusion-weighted (C and D, b = 1000 s/mm2) volume with the different phase encoding directions and gradient signs. The differences in the distortions between the AP and PA phase encoding directions can be appreciated most in the eyes (green arrows), temporal region (blue arrows), and the cerebellum (red arrows).

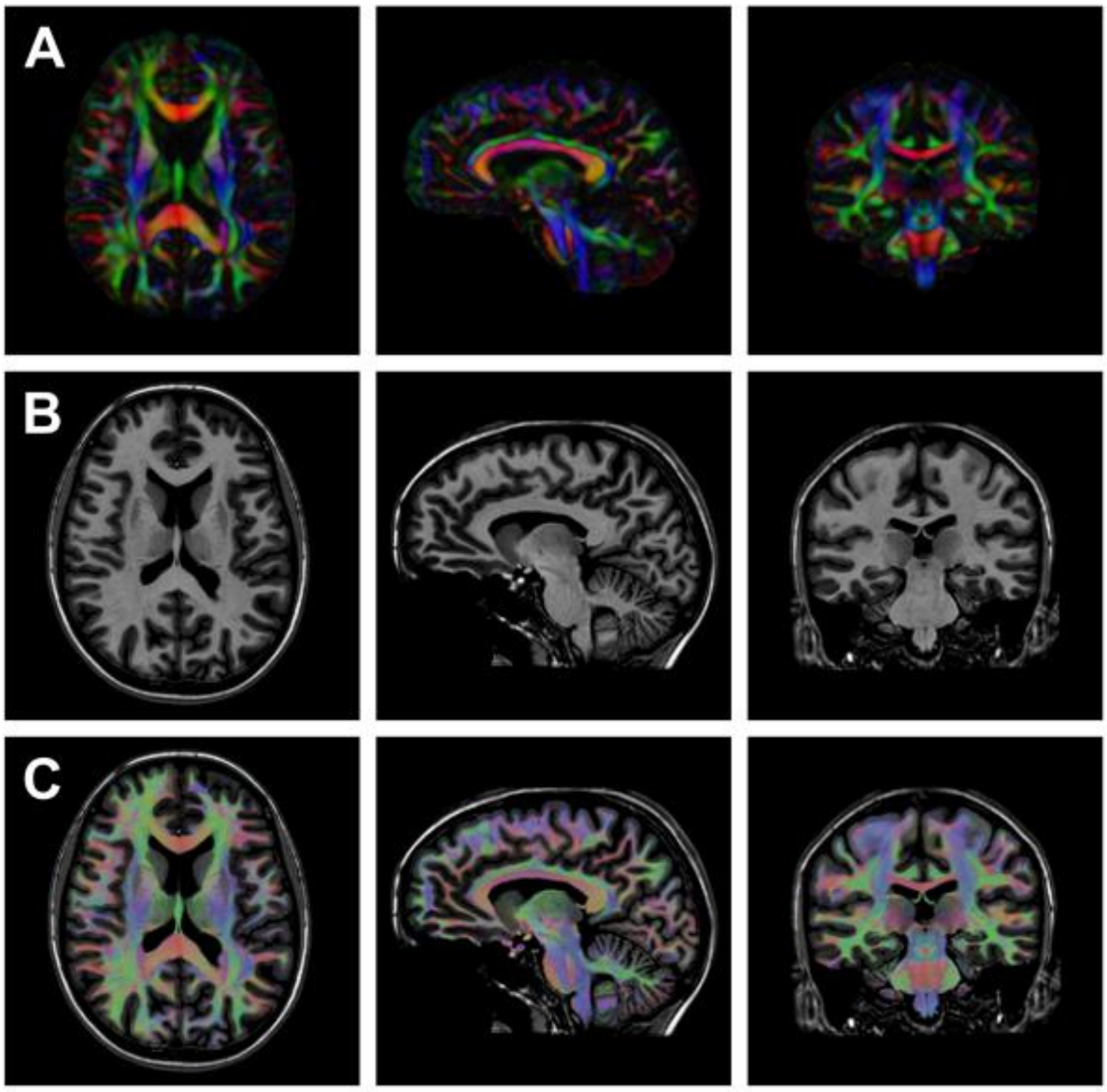

Figure 8: Example DTI reconstruction of the MASSIVE data. A) Color coded FA maps after applying all the correction procedures. B) T1 weighted data, which were used here to correct for EPI deformations. C) Color coded FA maps fused with T1 weighted data to appreciate the quality of the processing.

SUPPORTING MATERIAL

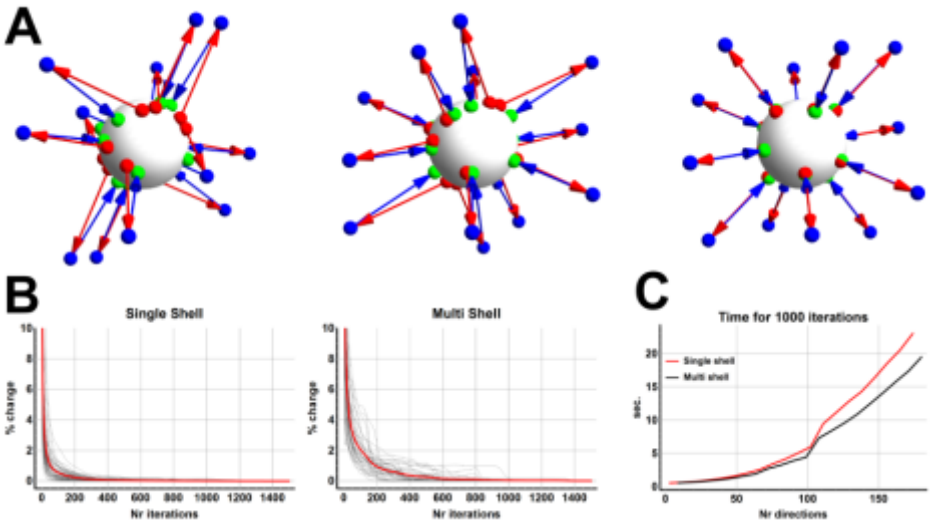

Figure S-1: A) Iterative method of optimization, first all particles are repulsed (red) after which they are projected back on the unit sphere (blue). The resulting particles (green) are then used for the next iteration. **B)** The percent change in entropy of the system over 1500 iterations for single- and multi-shell optimizations. **C)** Time it takes to perform 1000 iterations (Intel Core i5-2520M CPU, 2.5GHz) for shell ranging from 3 to 180 gradient orientations.

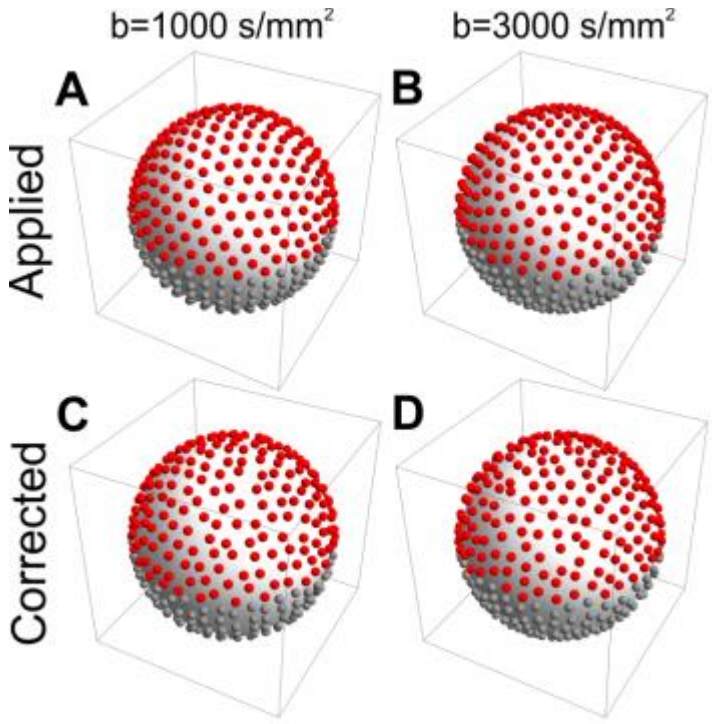

Figure S-2: Effect of subject motion on the imposed gradient orientations. The 500 gradient direction for b = 1000 s/mm^2 and b = 3000 s/mm2 as they were defined (**A** and **B**) and after registration with b-matrix correction (45) (**C** and **D**). The condition number of the b = 1000 s/mm^2 and b = 3000 s/mm^2 shells (1.5813 for both) changed to 1.5826 and 1.5861, respectively.